

## A STUDY OF NEUTRAL FINAL STATES IN $K^- p$ INTERACTIONS IN THE RANGE FROM 690 TO 934 MeV/c

D.F. BAXTER\*, I.D. BUCKINGHAM, I.F. CORBETT\*\*, P.A. DUNN,  
J. McL. EMMERSON\*\*\*, J. GARVEY†, F. HART, G. HUGHES\*,  
C.M.S. JONES‡, R. MAYBURY\*\*, N. MIDDLEMAS\*\*, P.R. NORTON‡‡,  
T.W. QUIRK, J.A. SCHEID and A.M. SEGAR

*Nuclear Physics Laboratory, University of Oxford*

Received 22 October 1973

**Abstract:** The  $K^- p$  reactions with final states  $\Lambda\pi^0$ ,  $\Sigma^0\pi^0$ ,  $\Lambda\pi^0\pi^0$ ,  $\Lambda\eta$  and  $\Sigma^0\eta$  have been studied at 14 momenta between 685 and 934 MeV/c using optical spark chambers. The charged decay products of the  $\Lambda$  are detected by low mass spark chambers while  $\gamma$ -rays from  $\pi^0$  and  $\Sigma^0$  decays are detected in high mass chambers. Approximately 250 000 photographs were analysed from which partial and differential cross sections were determined. These results are presented with an energy dependent, single channel partial-wave analysis.

### 1. Introduction

This paper presents the results of a study of the neutral final states in  $K^- p$  reactions in the kaon lab momentum range from 685 to 934 MeV/c. Data were taken at 14 momenta in this range for  $K^- p$  reactions into final states  $\Lambda\pi^0$ ,  $\Sigma^0\pi^0$ ,  $\Lambda\eta$ ,  $\Sigma^0\eta$  and  $\Lambda\pi^0\pi^0$ , all of which are pure isospin states. A difficulty in obtaining good data on the baryon resonances with strangeness-1 has been the clean separation of decay channels. Most of the data in this field has come from bubble chamber experiments, principally for the charged final states of mixed isospin [1–3] from which the data for pure isospin states must be derived. The pure isospin-1  $\Lambda\pi^0$  state, however, is seen in bubble chambers in  $K^- p \rightarrow \pi^0\Lambda$  and in the deuterium reaction  $K^- d \rightarrow \pi^-\Lambda$  ( $p$ ) with its special problems [4]. In the former case the  $\Lambda\pi^0$  events are extracted from the data by selecting on the basis of the missing mass associated with the  $\Lambda$  and this inevitably includes some contamination from other neutral channels. The

\* Department of Physics, University of Lancaster

\*\* Rutherford High Energy Laboratory, Chilton, Didcot, Berks.

\*\*\* University of Melbourne

† Department of Physics, University of Birmingham

‡ CERN, Geneva, Switzerland

‡‡ Daresbury Nuclear Physics Laboratory, Daresbury, Warrington, Lancs.

pure isospin-0 channel  $\Sigma^0\pi^0$  is not well studied in the hydrogen bubble chamber since the  $\Sigma^0$  decays to  $\gamma\Lambda$ , and  $\gamma$ -ray is not detected in the chamber. This reaction, as well as the other neutral final state reactions mentioned above, has been studied in the heavy liquid bubble chamber [5].

We have performed an experiment using optical spark chambers to detect both the  $\gamma$ -rays from  $\pi^0 \rightarrow \gamma\gamma$ ,  $\Sigma^0 \rightarrow \gamma\Lambda$  and  $\eta \rightarrow \gamma\gamma$  decays and the charged decay products of the  $\Lambda$ . The detection of all decay products enables us to separate final states by the number of  $\gamma$ -rays rather than by the missing mass technique resulting in relatively low contamination of the  $\Lambda\pi^0$  by the  $\Sigma\pi^0$  channel.

## 2. Experimental details

The general layout of the apparatus is seen in the cutaway view of fig. 1 and the plan view of fig. 2. The  $K^-$  beam was focussed onto a target of liquid hydrogen surrounded by spark chambers, wire chambers and scintillation counters. Closely surrounding the target was a scintillation counter operated in anticoincidence, so that

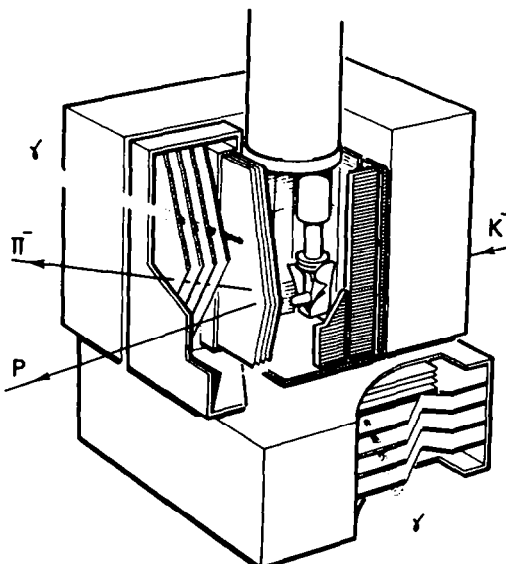


Fig. 1. Cutaway diagram of the apparatus. The beam enters from the right, passing through the upstream optical chambers and into the target which is surrounded on four sides and the bottom by spark chambers. Immediately enclosing the target is a veto scintillation counter, shown partly peeled away in this diagram. Both the thin foil plates and the thick plates of the optical chambers are represented here. The coincidence counters are shown lining the inside of the box formed by the optical spark chambers. The wire chambers, not shown in this drawing, surrounded the target in the region between the veto counter and the coincidence counters.

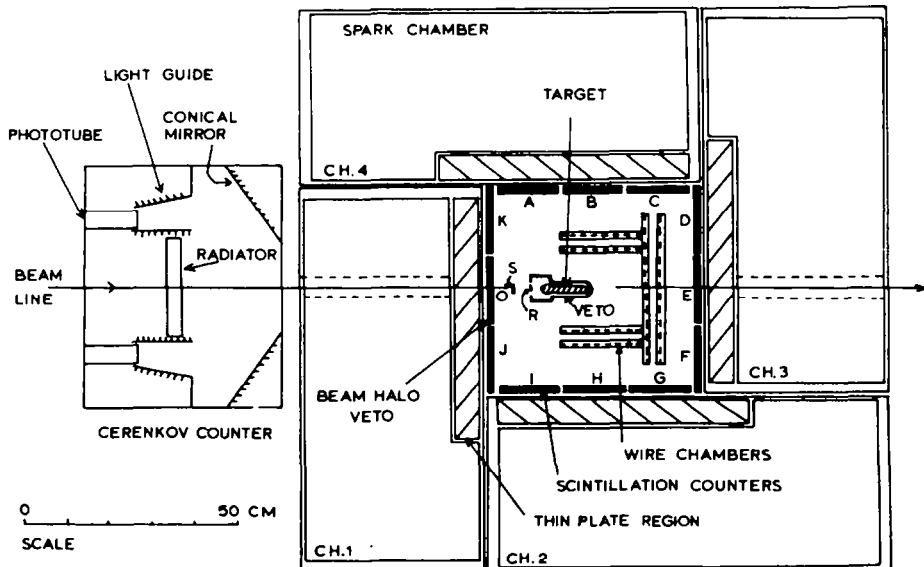


Fig. 2. Plan view of the apparatus.

only neutral reaction products were accepted from the target. The neutral particles of interest then decayed in the space between the veto counter and the spark chambers, and the decay products were detected in the spark chambers which were constructed so that charged particles and  $\gamma$ -rays were clearly distinguishable.

### 2.1. Beam

The primary target was situated in octant 4 of Nimrod and the particles produced at zero degrees were bent into the beam line by the accelerator field. The beam transport system included electrostatic separation, and vertical and horizontal collimation at an intermediate focus. The total length of the beam line from the internal target to the hydrogen target was 21.5 m corresponding to four  $K^-$  decay lengths at  $0.7 \text{ GeV}/c$ . The momentum acceptance of the beam was 1.5% fwhm and the beam spot, without intervening material, was  $2 \text{ cm} \times 1 \text{ cm}$  fwhm. The momentum of the beam was defined by a bending magnet in the second stage which was calibrated by the floating wire technique to an accuracy of 0.5%. Between the final quadrupole and the target there was a CERENKOV counter, an optical spark chamber, an optical spark chamber, two scintillation counters and the window of the target cryostat, making a total of  $6.5 \text{ gm}/\text{cm}^2$  of material traversed by the beam particle before entering the hydrogen. This meant that the kaon momentum at the target was 15 MeV/c below the nominal beam momentum, for the lowest momentum.

The magnification of the beam was approximately unity in both vertical and hor-

izontal planes. However, multiple scattering in the detectors in front of the target and the dispersive effects of the Nimrod fringe field gave a final spot size slightly larger than the two beam counters S and R (see fig. 2) which were 2 cm in diameter.

The number of particles other than kaons delivered to the target was between 20 and 40 times the numbers of kaons, depending on the momentum. The yield of kaons and the pion to kaon ratio at the secondary target for  $10^{12}$  protons incident on the primary target are given below for two lab beam momenta:

$P_L$ (GeV/c)	$K^-$	$\pi^-/K^-$
0.700	55	38
1.000	470	22

## 2.2. Counters and target

The partially separated incoming  $K^-$  beam was detected in a Čerenkov counter, Č, and two strobe counters, S and R. The beam was focussed onto a liquid hydrogen target surrounded by a veto scintillation counter. Five optical spark chambers formed a box which surrounded the target on four sides and the bottom; the top was left open and the target cryostat entered the box from above. The chambers covered 84% of the total solid angle from the target. The beam entered and left the apparatus through thin foil windows in the plates of the optical chambers, and entered the target through a hole in the veto counter.

The inside of the optical chamber box was lined with scintillation counters, hereafter called the coincidence counters. The central counter on the upstream chamber was an annular piece of scintillator through which the beam passed and which eliminated beam halo particles. Immediately surrounding the target was an assembly of low mass wire chambers with magnetostriuctive readout providing further information on charged particle tracks.

The trigger requirement was that a  $K^-$  was detected in the Čerenkov counter and in S and R, that there was no veto count, and that at least one of the coincidence counters fired. Thus the apparatus detected any one of the following final states:  $n\bar{K}^0$ ,  $\Lambda\pi^0$ ,  $\Sigma^0\pi^0$ ,  $\Lambda\eta$  (above 725 MeV/c),  $\Sigma^0\eta$  (above 889 MeV/c),  $\Lambda\pi^0\pi^0$ ,  $\Sigma^0\pi^0\pi^0$ . The distance from the target to the coincidence counters was less than 0.5 m which meant that the long lived  $\bar{K}^0$  state generally decayed outside the apparatus. The requirement that at least one of the coincidence counters fired meant in effect that only decays  $\Lambda \rightarrow \pi^- p$  and  $\bar{K}^0 \rightarrow \pi^+\pi^-$  triggered the system.

All channels considered in the final analysis were detected as two charged particles, the  $\pi^-$  and the proton from the  $\Lambda$  decay. Therefore the spark chambers had two distinct regions. The first, to detect the charged particles, had thin foil plates to minimize multiple scattering and maximize the particle range. The second region had 37 steel plates each 0.11 radiation lengths thick, the relatively thin plates giving high  $\gamma$ -ray conversion probability at high and low energies.

Apart from the normal requirement of high discrimination for K mesons, the Čerenkov counter was required to operate near the target where the particles were spread over an angular range of 50 mrad. Since the particles were themselves focussed at the target, ring focussing of the Čerenkov light was achieved with a conical surface mirror, not the usual parabolic.

The structure of the counter is shown in fig. 2. The radiators were cells of 3 cm thickness filled with a water and glycerol mixture having an index of refraction appropriate to the beam momentum. The position of the cell relative to the mirror was remotely controlled to allow optimization of the selected angle at each momentum. The Čerenkov light was viewed through the conical mirror by eight RCA 8575 photomultipliers placed at the ends of light collecting cones. The trigger required an eightfold coincidence.

The angular response of the counter was verified at the CERN synchrocyclotron using a pencil beam. The efficiency and rejection were measured in the Nimrod beam, as seen in fig. 3. The efficiency of the eight-fold coincidence for kaons was 90%, and the rejection for pions and muons on the kaon peak was about  $10^{-4}$ , and better at the pion peak. With a  $\pi + \mu$  to K ratio of about 40, the pion background in the beam count was less than 1%.

The target dimensions were a compromise between the following requirements. Firstly, it was a requirement of the trigger that the lambda decayed outside the veto. The short lifetime of the lambda caused a large drop in detection efficiency for lambdas of low momentum in the laboratory. Secondly, considerations of the event rate, event to background ratio and the difficulty in obtaining a large K beam phase space within a small target volume all suggest a target volume as large possible. These considerations lead to a choice of target dimensions of 11 cm long tapering from 1.8 cm diameter to 1.2 cm diameter at the downstream end. The vessel itself was constructed of mylar 0.005 inches thick. Surrounding the target was an aluminium vacuum vessel whose walls were 0.030 inches thick.

The small size of the target required a small final beam spot. It also required careful positioning of the beam defining counters to ensure maximum target illumination. Two discs of scintillator 2 cm in diameter and 0.32 cm thick formed the two beam counters S and R. They were fixed to the target support and were approximately 1.5 and 4 cm from the target entrance. Air light guides were used since particles scattering out of the beam passing through perspex light guides and triggering the counters by Čerenkov radiation were likely to miss the veto counter and thus increase the background. With 3 mm thick scintillator there are  $0.13 \text{ gm/cm}^2$  of protons (of which 86% are bound) in the final strobe compared to  $0.7 \text{ gm/cm}^2$  in the liquid hydrogen target. So although this produced a substantial background it was tolerable. Position information for the incoming beam particles came from the optical chamber through which the beam passed before hitting the strobes. The error on the determination of the direction was  $\pm 10$  mrad. Strobes 3 mm thick produce multiple scattering with an rms of 1.5 mrad for a kaon of  $700 \text{ MeV}/c$ , so that this effect on the beam particle direction could be ignored.

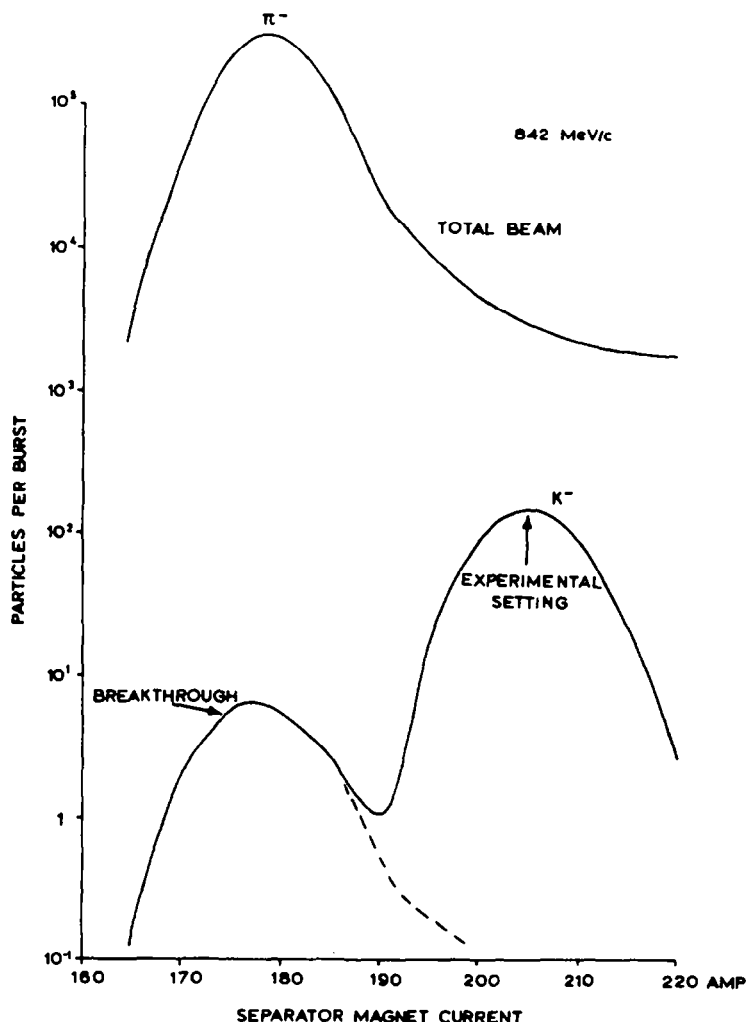


Fig. 3 Cerenkov counter performance. Pions and kaons per burst at beam momentum 842 MeV/c are plotted against the separator magnet current.

The efficiency of the veto counter was crucial to the experiment because the rate of interactions that produced neutrals was about  $1.0 \times 10^{-3}$  per incident kaon. (The cross-sections are 22 mb for charged outgoing channels and 8 mb for neutral outgoing channels at 700 MeV/c). The veto counter therefore enclosed the target vacuum vessel as closely as possible and was made of the thinnest scintillator (3mm) compatible with a failure rate much less than 1 in  $10^3$ . In order to fit the target closely, it was made in the shape of a box with a conical snout which surrounded

the long conical target. Light was collected from all sides of the veto counter box and guided to an RCA 8575 photomultiplier tube.

A detailed investigation of the efficiency of the target veto counter was made both in the laboratory with a source and with the experimental beam. Measurements of pulse heights from various parts of the scintillator indicated that the light collection efficiency of the scintillator plus light guide varied from about 5% to 20%, so that minimum ionizing particles traversing the counter produced some 300 photons at the photocathode. The electronic logic for the veto counter was carefully designed and incorporated a duplicated feature to inhibit the system for 20 ns after a veto signal, covering the deadtime of the veto counter and allowing the electronics to recover from large veto pulses. The result of tests in the pion beam showed that in no part of the scintillator was the vetoing efficiency less than 99.995%.

The fence of coincidence counters which lined the box of optical chambers consisted of eleven vertical paddles 20 cm  $\times$  60 cm labelled counters A to K (fig. 2) and one larger counter, counter L, which rested on top of the bottom chamber. These were made of 0.63 cm thick scintillator mounted on 56 AVP photomultiplier tubes. Their purpose was to signal the charged decay of the lambda (or neutral kaon) inside the decay volume. They were required to be of uniformly high efficiency in order that no biases were introduced into angular distributions. However, since there were two charged particles in all events of the final data and since the trigger only required a signal from one counter, the single particle detection efficiency of a counter was not critical.

The thickness of the counters was important for three reasons. Firstly,  $\gamma$ -rays could convert or neutrons produce a recoil to simulate charged particles and trigger the system. For a 100 MeV  $\gamma$ -ray the counter represented 0.015 of a conversion length. This produced background triggers from  $\Lambda \rightarrow \pi^0 n$ ,  $K^- p \rightarrow K^0_s n \rightarrow \pi^0 \pi^0 n$  and  $K^- p \rightarrow K^0_L n$  and these events appeared with any number of  $\gamma$ -rays and no charged particles or one charged particle. Events in these categories represented a large fraction of the background triggers in this experiment. Secondly, multiple scattering of the charged particles before entering the optical chambers degrades the data. This is most important for low energy protons. Finally, the counters and wire chambers imposed an absolute cut-off of 212 MeV/c for protons and 55 MeV/c for pions as the lowest momenta above which particles reached the optical chambers. Since events measured were selected on the basis of two charged tracks being seen in the optical chambers, events with particles below their appropriate cut-off momentum were lost to the analysis. The loss of the low momentum protons was most serious since they were from low momentum lambdas and so concentrated in a particular part of the angular distribution, whereas the low momentum pions were spread fairly uniformly through the angular distribution.

Thus the coincidence counters were made as thin as possible, consistent with a single counter efficiency of greater than 90% which gave a probability of detecting at least one of the particles of greater than 99%.

### 2.3. Wire and optical chambers

The four magnetostrictive wire chambers placed in the decay volume between the veto and coincidence counters were of very low mass ( $0.18 \text{ gm/cm}^2$ ) in order to minimize the energy loss and multiple scattering of slow protons passing through them. Their purpose was to add spatial information on the charged particles tracks to that obtained from the optical chambers. Since most of the lambdas decayed near the target, there was a long lever arm from the optical chambers to the decay point so that the determination of the interaction point was improved by these chambers. The experimental resolution was 0.5 mm. The wire chamber data were recorded on magnetic tape and could be optionally added to the optical data.

The optical chambers were required to detect, differentiate and provide information on the energy of charged particles and  $\gamma$ -rays. Each chamber was a gas tight perspex box containing 44 nickel-plated steel sheets of thickness 0.11 radiation lengths. The plate area was 78 cm  $\times$  86 cm for the side chambers and 109 cm square for the bottom chamber. Alternate plates were pulsed to about 10 kV with intervening plates held at earth. These pulses were derived from a series of spark gaps and arrived at the plates about 400 ns after the event. For  $\gamma$ -rays travelling normally to one of the chambers there was a total of 3.6 radiation lengths of steel giving a conversion probability of 95%.

The first seven plates of each chamber had rectangular holes cut in them which had 0.025 mm thick aluminium foil backed with polystyrene foam stretched across them. Corresponding holes were made in the perspex chamber faces and the windows sealed with thin mylar sheet. These holes were positioned to cover most of the detection solid angle visible from the target. The charged particles were seen in these gaps and were distinguished from  $\gamma$ -rays which showered at a greater depth into the chambers.

The plate spacing was maintained at 0.81 cm across the face of each plate by four assemblies of perspex insulators threaded on rods passing through the chambers. The chambers were continuously flushed with a 70–30 mixture of neon-helium at slightly above atmospheric pressure. Cosmic ray tests of the efficiency of the chambers were made on completion of each chamber, and during and after data taking. For tests made after data taking, giving the lowest results, the thin foil efficiencies were on the average 85% per gap and the steel plate average efficiency was 90% per gap. The loss of efficiency was attributable to spark robbing due to breakdown which developed during the use of the chambers. Tests were also made to optimize efficiency as a function of clearing field voltage and time delay in applying the pulsed voltage.

The chambers were viewed normally from two directions through perspex lenses mounted on the chamber faces. The ten views were brought to the camera by a system of 52 mirrors. Perspex plates engraved with two sets of fiducial patterns were mounted on each view. One set, mounted on the front and back of each view, was illuminated for a few frames on every roll of film. The other set, mounted only on

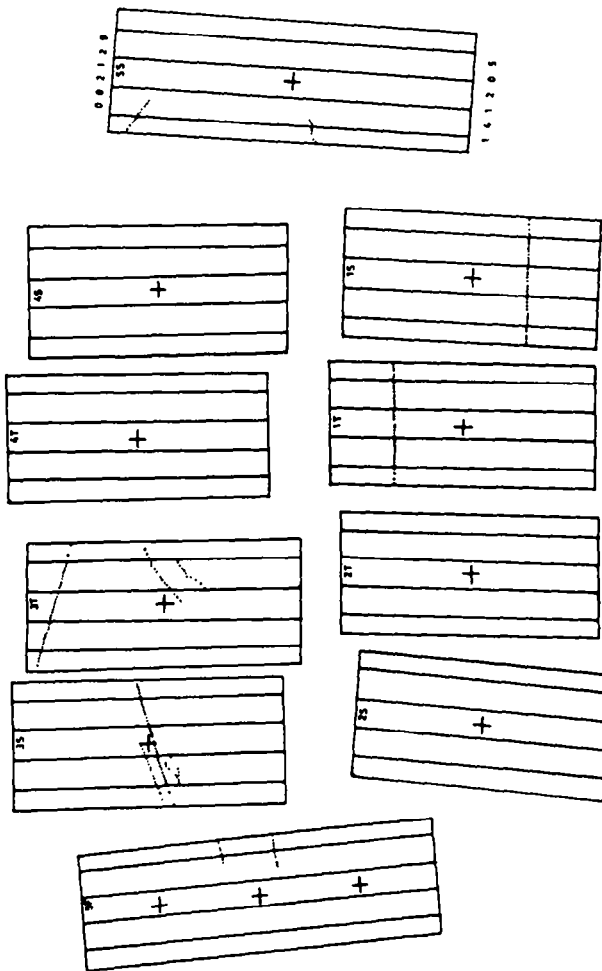


Fig. 4 A representative event frame. This is a drawing made from a picture taken for beam momentum 898 MeV/c. The top and side views of the five chambers are labelled 1T, 1S etc. The event is interpreted as  $K^- p \rightarrow \pi^0 \Sigma^0$  followed by the decays  $\pi^0 \rightarrow \gamma\gamma$ ,  $\Sigma^0 \rightarrow \gamma\Lambda$  and  $\Lambda \rightarrow \pi^- p$ . The beam track is seen in chamber 1, the upstream chamber; the two charged tracks and one gamma are in chamber 3, the downstream chamber, the other two gamma rays are seen in chamber 5, the bottom chamber.

the front, was illuminated on each trigger by flash tubes operated by a pulse derived from a secondary spark gap. Trigger pulses were employed to illuminate the run and frame numbers on scalers which were also recorded on the film thereby labelling every event. Each picture was recorded with a 35 mm Flight Research camera, both Kodak and Adox film being used. A representative frame is shown in fig. 4.

#### 2.4. Electronics

The electronic logic which selected good events and monitored many other rates was built from the Rutherford Laboratory Tunnel Logic System. The signal cable lengths from the photomultiplier tubes were adjusted so that all signal pulses from a good event arrived in coincidence at the digitizing units of the logic. The two beam counters S and R in coincidence generated strobing pulses which were gated by all other counter signals. The eight Čerenkov tubes were combined in coincidence ( $\bar{C}$ ) to indicate a kaon in the beam. The counters O and V were in anticoincidence and the combined signal  $SR\bar{O}V$  indicated a beam particle with neutrals leaving the target. The coincidence counters A to L were combined into a COINC signal with OR gates thus signalling a particle in any of the counters. The final trigger was thus  $SR\bar{O}V \bar{C}$  COINC. The veto counter was protected against particles arriving within the deadtime of the electronics.

The primary control of the system was a main gate which permitted counting for a period of 550 ms during which there was Nimrod flat top with spill onto the internal target. Further inhibiting gates were set by separator breakdown, film end or breakage, and the spark chamber trigger. A period of 160 ms was required for the power supplies to recharge the storage capacitors on the spark gaps. The Nimrod spill of 550 ms and our deadtime after a trigger of 160 ms permitted three triggers per burst. At low momenta ( $700 \text{ MeV}/c$ ) typical trigger rates were one per ten beam bursts, rising to one per beam burst at  $1.0 \text{ GeV}/c$ . Hence the deadtime did not significantly slow down data taking.

#### 2.5. Data collection

At the beginning of each run the optical layout was checked by taking photographs of the fiducial grids. At the same time a visual check was made. During the runs the rates were regularly monitored. The performance of spark gaps was monitored on scalers in the control room. At the end of each run the scaler information was recorded, and the efficiency of the Čerenkov counter, the effective spill time, the system deadtime and other quantities were calculated which provided a sensitive check on the performance of the apparatus. From the end of each roll of film a test strip was removed and processed immediately as a further check on the performance of the optical system.

## 2.6. Survey

Careful surveys of the chambers were performed to determine their relative positions. Since charged particle tracks frequently intersected two chambers, the positions of the chambers had to be known to an accuracy of better than 1.5 mm, the resolution of the measuring system in chamber space. A survey procedure was designed which gave a relative chamber position accuracy of 1 mm using two approaches. In the first, engraved perspex survey grids were placed across two spark chambers and photographed against the fixed fiducial grids of the chambers. By fitting the reconstructed values of the survey grid engravings to the known positions on the grid, the relative positions of the projections of the views were determined. This method, however, left undetermined the angle of rotation of each chamber about the axis perpendicular to the chamber plates, and this was measured directly.

In the second method, the system was triggered on cosmic rays. By using various combinations of coincidence counters, cosmic rays were selected linking adjacent chambers. These events were photographed and processed, and points in the chamber space were fitted to straight lines joining the chambers. While determining all parameters, this method depended on our knowledge and treatment of the chamber distortions. A careful examination of many sets of data from both survey methods provided sensible agreement at the 1 mm level.

## 3. Data processing

The period of Nimrod time allocated to this experiment permitted the taking of about 16 000 frames of data at each 20 MeV/c momentum interval in the range from 685 to 934 MeV/c. Target full and empty runs were alternated and typically consisted of some 2400 target full frames followed by 600 target empty frames so that about 20% of the triggers were used for background subtraction. The data were collected on rolls of 3200 frames with the counter and wire chamber data recorded on corresponding magnetic tapes.

### 3.1. Scanning and measuring

The film was scanned for various categories of events. Any track starting in the four active gaps in the thin foil regions of the chamber was called a charged particle and the tracks appearing at a greater depth were defined as  $\gamma$ -rays. The minimum requirement for both categories was that the track possess three visible sparks within four gaps. The scanner noted the number of incoming and outgoing beam tracks and the numbers of charged particle and  $\gamma$ -ray tracks. Tracks that were obviously stale, most frequently occurring in beam tracks, were omitted from the scan. This information was recorded on paper tape and the results of two such independent scans were compared to produce a list of events with differing scan information.

where at least one scanner had seen the minimum requirement of four tracks, two charged tracks and two  $\gamma$ -rays. A third scan decided which if either of these was correct. A collation then produced a 'call tape' of events with at least four tracks which were passed on for measurement.

Thus the film had been triple-scanned for events of the measurable categories. The apparent scan efficiency, deduced from the inconsistencies, between scans, was high. Still we were not satisfied that all candidates had been seen, and tried a super scan of a sample of the film with careful examination of each frame for possible additional tracks. Most new tracks found were rubbish, but some proved to be very faint or obscured tracks belonging to good events. For the  $\Lambda\pi$  channel we obtained in this way a scan efficiency of  $0.77 \pm 0.04$ ; for the  $\Sigma\pi$  channel it was  $0.77 \pm 0.07$ . The loss is appreciable, but since it is concerned with faint tracks, it shows no angular bias and we have applied it as a correction with error to all the results we quote.

In measuring frames selected by the call tape, the operator first located the frame by measuring the coordinates of the fiducial crosses at the centres of the ten views. For the beam track, the first spark and the last five sparks were measured. For scattered charged particle tracks, the first five sparks were measured and also the last spark visible in both views. For gamma rays, the conversion point or the first point visible in both views and the end point of the shower were measured. Coupled with the interaction point, this tied down the  $\gamma$ -ray direction more tightly than measurements from the shower; and it gave some information on the energy through the track length. These measurements went directly onto magnetic tape and were passed to the geometry program for reconstruction. A set of chamber view parameters, namely the positions of the central fiducial cross and four corners of each view, were measured at least once per roll of film.

Tracks were then reconstructed in real space using the survey data in a program which corrected for optical distortions. The parameter set was also checked by this program and a warning was given if there was an indication of systematic shifts due to a mirror movement.

### 3.2. Kinematic fitting and cuts

As a preliminary to kinematic fitting, some sorting of measured tracks was needed. If more than two charged tracks had been seen in scanning, it was determined whether any of these could have been derived from  $\gamma$ -rays. Showers that extended into a second chamber or had a break of more than ten gaps had been processed as two separate  $\gamma$ -rays. Therefore at this point tracks inclined at less than  $10^\circ$  were combined.

The data in this form were then passed to a kinematic fitting program. A generalized least-squares method was used for kinematic fitting, with iterative minimization of a  $\chi^2$  function subject to constraints. The function minimized with respect to  $m$ ,  $x$  and  $\alpha$  was

$$\chi^2 (m, x, \alpha) = (m - m_0)' G^{-1} (m - m_0) + 2\alpha' f(x, m), \quad (1)$$

where  $G$  is the error matrix,  $x$  is the vector of unknown variables,  $m_0$  is the vector of initial values of the measured quantities,  $m$  is the vector of values of the measured quantities as they vary in the fit,  $\alpha$  is a vector of Lagrange multipliers and  $f(x, m)$  are the residuals of the constraint equations.

In the case of the  $\Lambda\pi^0$  final state:

(i) Measured variables used were 18; (a) kaon momentum and points on its track given as  $(x, y)$  coordinates at two fixed  $z$ -planes normal to the beam, (b) V intersection point of the pion and proton tracks plus  $(x, y)$  coordinates at two planes for each of the latter tracks, (V fitting and calculation of an error matrix for this fit was a preliminary to the overall kinematic fitting.) (c)  $\gamma$  conversion points  $(x, y, z)$ .

(ii) Unknown variables used were 9; (a)  $z$  coordinate of the interaction point along the beam, (b) momenta of the  $\Lambda$ ,  $\pi^0$ ,  $\pi^-$ ,  $p$ ,  $\gamma_1$  and  $\gamma_2$ , (c) azimuthal and polar angle of the  $\pi^0$ .

(iii) Constraint equations were 12; (a) momentum and energy balance at the interaction point, (b) the same for the  $\Lambda$  decay point, (c) the same for the  $\pi^0$  decay point.

We see that the fit was overdetermined, of the three constraint type. Similar combinations of variables were used for the other channels, and the  $\Lambda\eta$ ,  $\Sigma^0\pi^0$  and  $\Sigma^0\eta$  are 3 C fits, while the  $\Lambda\pi^0\pi^0$  is 2 C. There was additional measured information in the form of particle ranges and knowledge of the position of the interaction volume, but this was used in cutting after the fit.

A multi-vertex fit of this kind is inclined to give convergence difficulties due to the lack of linearity in any of the variables involved. We chose our variables, using a Monte Carlo event generating program for testing fitting efficiency, to minimize such difficulties. Also, the iteration procedure was protected in the usual ways. Most important also in achieving a high fitting efficiency was the calculation of starting values for the fit. After the V fit, the constraint equations were used in a minimization to calculate accurate starting values. At this stage it was also possible to decide, in most cases, which of the two charged tracks was the proton. Ambiguous cases could be sorted later in cutting.

Output from the fitting program consists of fitted variables with errors for one or more of the hypotheses  $K^- p \rightarrow \Lambda\pi^0$ ,  $\Sigma^0\pi^0$ ,  $\Lambda\eta$ ,  $\Sigma^0\eta$  and  $\Lambda\pi^0\pi^0$  with  $\Lambda \rightarrow \pi^- p$ ,  $\Sigma^0 \rightarrow \Lambda\gamma$ ,  $\pi^0 \rightarrow \gamma\gamma$  and  $\eta \rightarrow \gamma\gamma$ .

Four types of cuts were then applied to the fitted data. The cuts were such that they had maximum effect on the target empty rate and minimum effect on the hydrogen signal. First, a high proportion of the background events had chi-squared probability of less than 5% and so the cut after the kinematic fit was set to this level.

Secondly, a cut was made on the range of the charged particles. When the fitted particle momentum was substantially lower than the momentum estimate derived from the track length, the event was rejected. The margin was set at 50 MeV/c for both pions and protons. Besides having a considerable effect on the background,

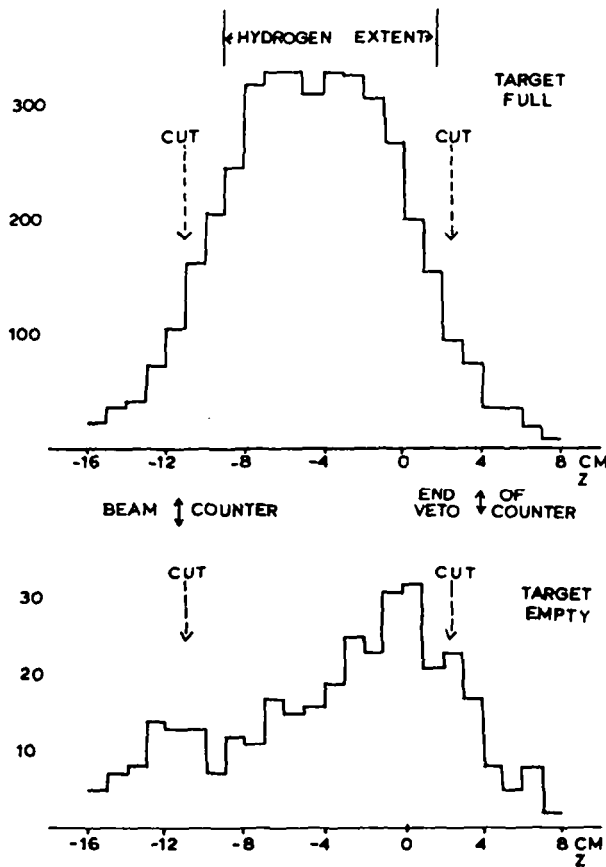


Fig. 5. The interaction point distribution along the length of the target plotted for fitted events from target-full and target-empty runs.

this cut reduced to 2% the number of events in which the identification of the pion and proton was ambiguous.

Thirdly, a cut was made on the interaction volume, rejecting events arising from the strobe counters. The interaction point distributions for target full and empty are shown in fig. 5 with the final limits imposed.

The final cut was made on the  $\pi^0$  opening angle. If the opening angle in the centre of mass was greater than the kinematically allowed minimum by an amount such that  $\cos \theta_{\min} - \cos(\gamma_1, \gamma_2) > 0.85$ , the event was discarded. The proportion of good events that would have been rejected of the  $\gamma$ -ray detection were uniform with energy was 5%. This fraction had wide opening angles and a low energy  $\gamma$ -ray, and therefore many of them were undetected in the apparatus. A Monte Carlo investigation showed that fewer than 1% of good measured events were lost through this cut.

After applying the cuts, a background subtraction was performed. The target-full

and target-empty data were carried through the analysis in exactly the same way producing signal and background distributions and at this point the target-empty distributions were subtracted from the target full distributions removing about 5% of the events. In the final data set there were 2100  $\Lambda\pi^0$  events and 600  $\Sigma^0\pi^0$  events after all subtractions.

#### 4. Detection efficiency

We include in the overall event detection efficiency those efficiencies that arose in the data analysis mentioned previously. These factors were dependent not only on the event topology, but also on the information conveyed to the fitting program. To determine the overall efficiency, therefore, the experiment was simulated in a Monte Carlo program which generated events that would have satisfied the scanning and measuring criteria and these were put through the analysis in the same format as the data. The fitting program efficiency was tested, using the Monte Carlo simulated data, for all factors that might be critical to its stability, but in no case was any particular dependence found. The final success rate for simulated events determined the detection efficiency.

The main effect producing a non-uniform detection efficiency was the propor-

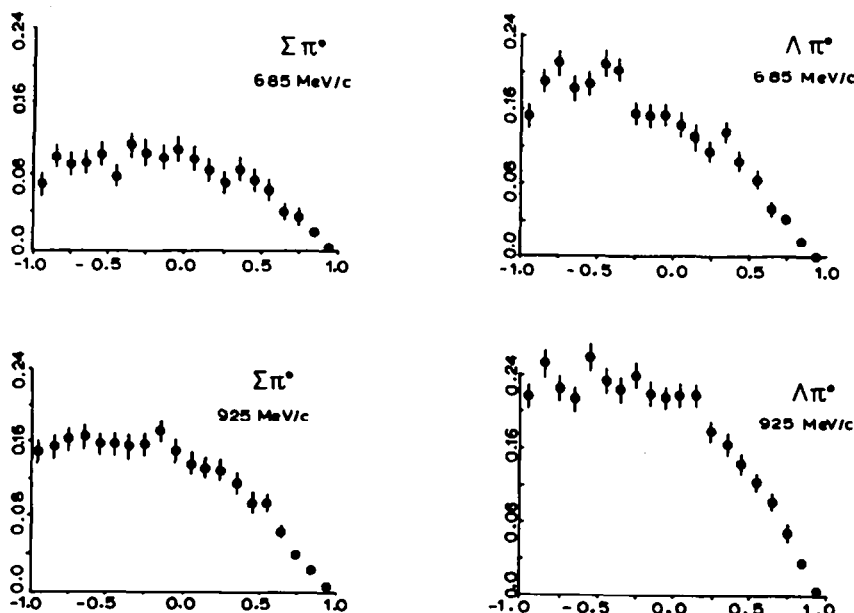


Fig. 6. The overall apparatus efficiency plotted against the centre of mass angle between the initial kaon and final pion for the  $\Lambda\pi^0$  and  $\Sigma^0\pi^0$  channels at 685 MeV/c and 925 MeV/c.

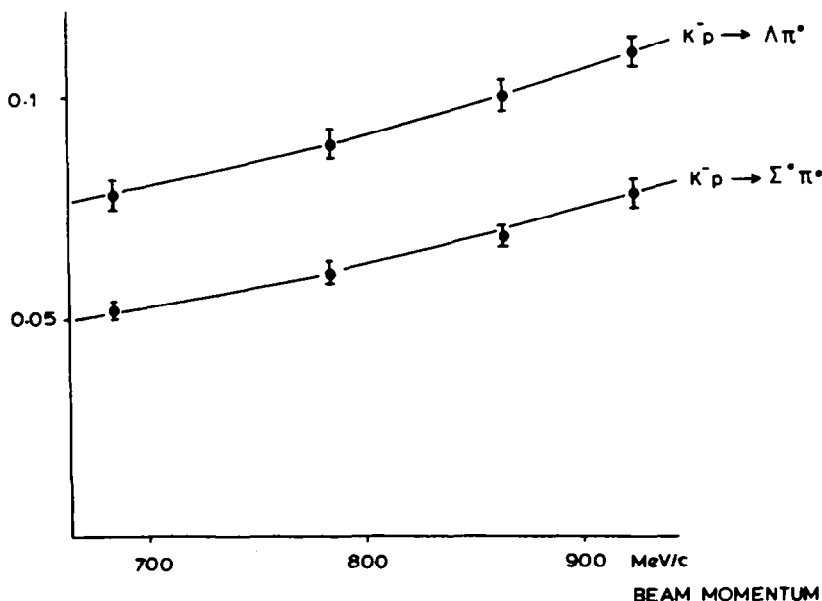


Fig. 7. The overall detection efficiency averaged in the centre of mass system plotted against beam momentum.

tion of events for which the lambda decayed within the veto counter. The loss of events in the backward scattering was particularly severe since in these events the hyperon had small forward lab momentum and decay length. The other significant factor in charged particle detection was the proton range. There was an absolute momentum cut-off at 0.212 GeV/c due to the proton failing to pass through the material of the wire chambers and scintillator. Thus, the chance of detecting a slow proton from a backward going lambda dipped sharply as the angle between the  $K^-$  and  $\pi^0$  approached  $0^\circ$ .

The principal effect in determining the  $\pi^0$  detection efficiency was the geometrical deployment of the steel, the loss of  $\pi^0$  being almost entirely caused by the hole in the top of the apparatus. This gave an overall geometrical loss due to particles missing chambers.

Systematic effects considered in this simulation were the variation of conversion length with energy, which was slight, and the shower length as a function of energy and angle. The spark production efficiencies used were taken from studies done on similar chambers in a previous Oxford experiment. Any departure from this would be serious only for low energy  $\gamma$ -rays and the fraction of events with  $\gamma$ -rays of energy less than 40 MeV/c, where the production efficiency began to fall steeply, was very small. We show the overall apparatus efficiency for the possible final states in

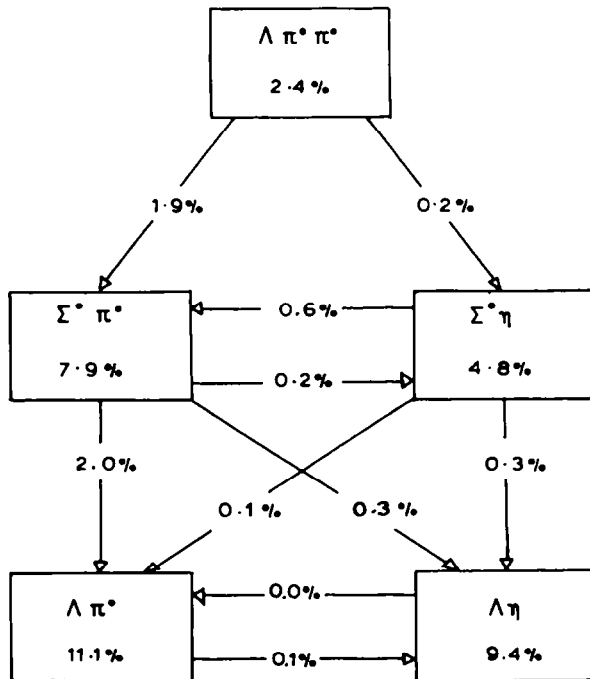


Fig. 8. The figures in the boxes represent the accepted fraction of the total number of events generated of the type indicated by the box label. The figures in the arrows are the fractions of events of that type which fitted the type of event indicated by the arrow. All figures are for a beam momentum of 925 MeV/c.

fig. 6. The overall detection efficiency averaged in the centre of mass system is shown as a function of beam momentum in fig. 7.

With a  $\gamma$ -ray detection efficiency less than 100%, there were some events having three gammas, for example, in which one gamma was lost and the event fitted another topology. Thus, there was feed-down from the  $\Sigma^0\pi^0$  channel to the  $\Lambda\pi^0$  and  $\Lambda\eta$  channels and from  $\Lambda\pi^0\pi^0$  to  $\Sigma^0\pi^0$ . The interchannel contamination was calculated from Monte Carlo events and is summarized in fig. 8 for a beam momentum of 925 MeV/c.

Since the final results depend upon the overall efficiency as calculated by the Monte Carlo program, it is important to check this calculation. To do this the Monte Carlo results were compared to some data distributions which we now consider. The most sensitive of these checks was the particle momentum spectra which showed agreement between data and Monte Carlo results for pions (fig. 9), protons and  $\gamma$ -rays.

We have also checked the charged particle behaviour by calculating the  $\Lambda$  lifetime. The effect of the detection process is contained in a correction factor shown in

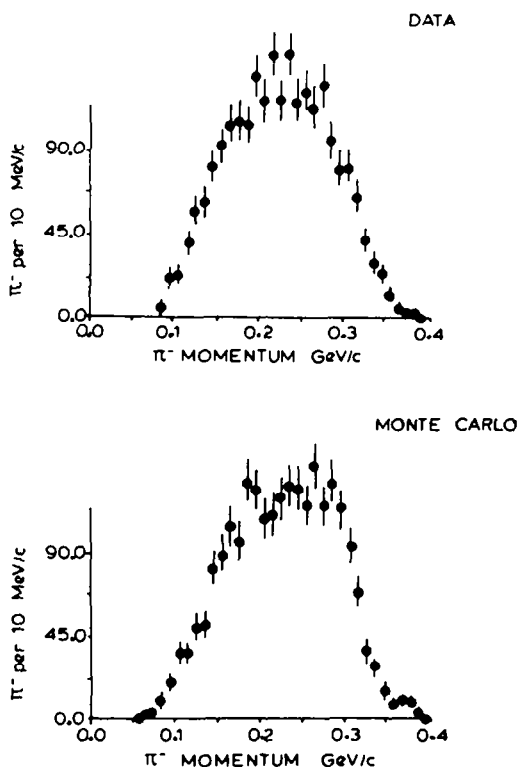


Fig. 9. The pion momentum spectrum from data and Monte Carlo calculations.

fig. 10 which was determined from the departure of the Monte Carlo lifetimes from an exponential distribution. The corrected lifetime distribution is shown in fig. 10 from which our estimate of the lifetime is  $(2.33 \pm 0.40) \times 10^{-10}$  seconds in agreement with the world average of  $(2.521 \pm 0.021) \times 10^{-10}$  seconds [6].

## 5. Results and analysis

### 5.1. Normalization

The normalization of the data depends on the target illumination, that is, the fraction of the total length of the 11 cm of liquid hydrogen that an average beam particle traversed. The target illumination was first calculated to normalize the data of this experiment for the reaction  $K^- p \rightarrow \Lambda \pi^0$  to that given by the CHS collaboration [1, 2]. This required an illumination of 0.51 calculated by taking a weighted mean of the ratio of the number of hydrogen events in the experiment to the CHS cross section for the region  $-1.0$  to  $+0.8$  in the cosine of the cm angle.

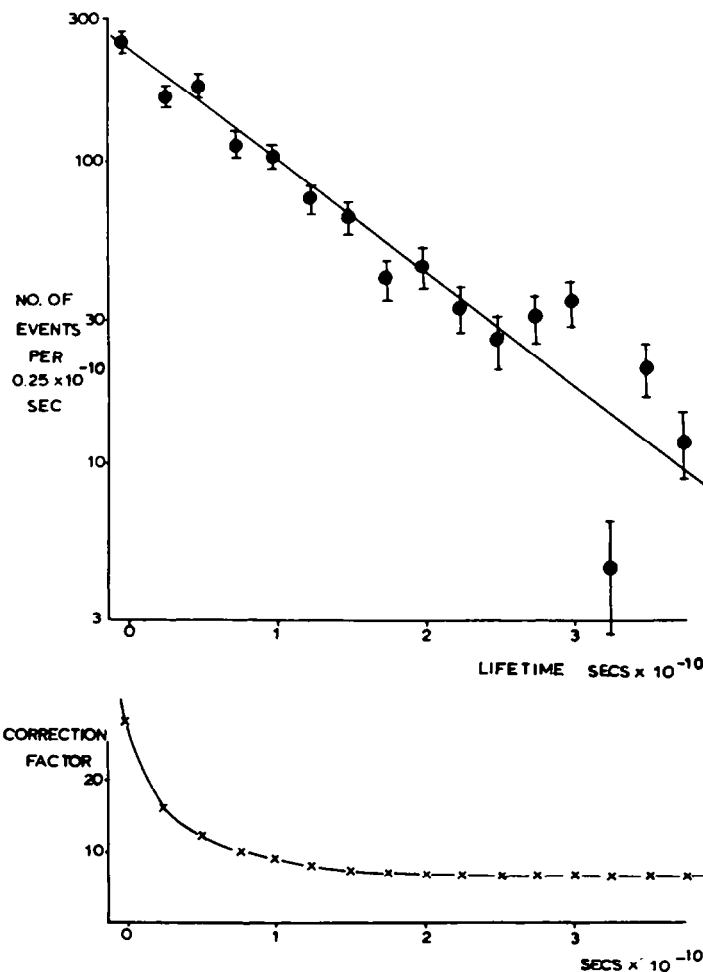


Fig. 10. The lambda lifetime and the correction factor determined from the departure of the Monte Carlo lifetimes from an exponential distribution.

The target illumination was independently determined from the experimental data from a consideration of the rate for interactions on hydrogen that produced no veto signal and did not trigger the apparatus. These neutral final states did not decay into charged products between the veto counter and the coincidence counter fence. The processes that can cause no veto signal and will not trigger the apparatus are

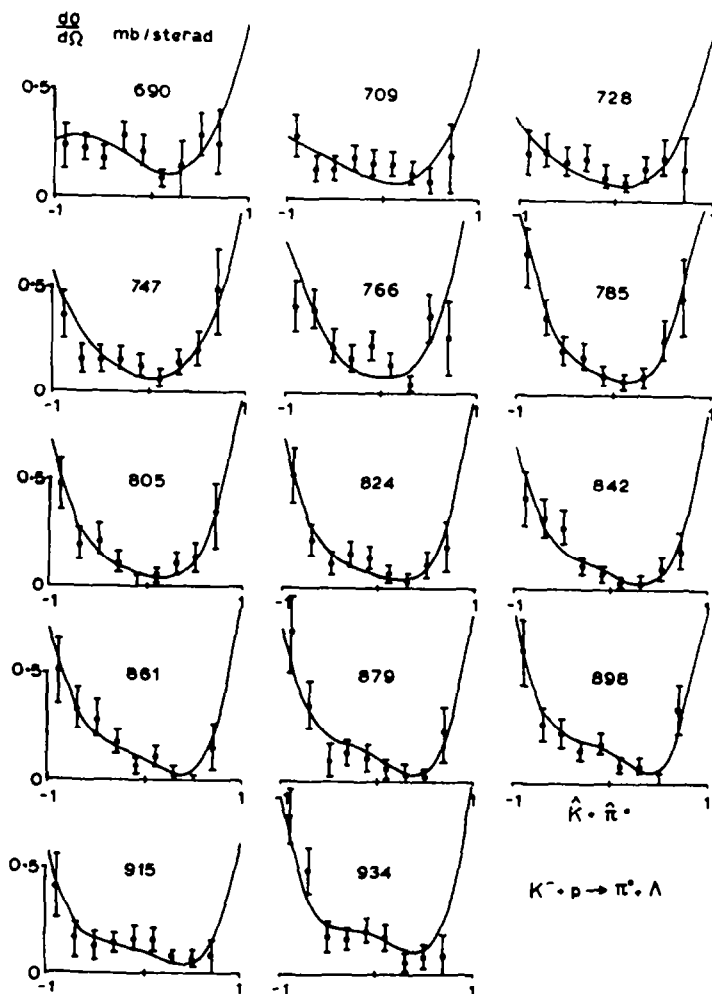


Fig. 11. The differential cross section for the  $\Lambda\pi^0$  channel. The curves are from the partial wave solution.

$K^- p \rightarrow \bar{K}_L^0 n$   
 $\rightarrow \bar{K}_L^0 \pi^0 n, \quad \pi^0 \rightarrow \gamma\gamma,$   
 $\rightarrow \pi^0 \Lambda, \quad \Lambda \rightarrow \pi^0 n,$   
 $\rightarrow \pi^0 \Sigma^0, \quad \Sigma^0 \rightarrow \gamma\Lambda,$   
 $\rightarrow \eta\Lambda, \quad \eta \rightarrow \gamma\gamma, \gamma\gamma\pi^0, 3\pi^0$   
 $\rightarrow \Lambda + \text{ neutrals (2 or more } \pi^0).$

Table 1

Differential cross section for the reaction  $K^- p \rightarrow \pi^0 \Lambda$  as a function of the cosine of the c.m. scattering angle between the initial kaon and the final pion momenta and at fixed values of the  $K^-$  lab momentum,  $p_L$ . The bin width in  $\cos \theta_{cm}$  is  $\pm 0.10$ . The error is given beneath the value of the cross-section for each entry. The cross section is given in mb/stir

$p_L$ (MeV/c)	-0.9	-0.7	-0.5	-0.3	-0.1	+0.1	+0.3	+0.5	+0.7
690	0.191	0.185	0.148	0.230	0.175	0.067	0.114	0.240	0.212
	0.087	0.051	0.047	0.054	0.053	0.032	0.048	0.084	0.123
709	0.226	0.111	0.110	0.149	0.131	0.128	0.094	0.070	0.154
	0.080	0.048	0.045	0.044	0.048	0.044	0.044	0.046	0.126
728	0.168	0.181	0.140	0.155	0.087	0.063	0.114	0.159	0.107
	0.077	0.056	0.047	0.045	0.040	0.030	0.043	0.064	0.117
747	0.267	0.118	0.115	0.118	0.089	0.043	0.105	0.154	0.354
	0.083	0.047	0.046	0.040	0.039	0.029	0.041	0.059	0.153
766	0.295	0.294	0.164	0.118	0.165	0.099	0.034	0.262	0.187
	0.090	0.070	0.056	0.046	0.052	0.043	0.031	0.083	0.122
785	0.475	0.267	0.149	0.137	0.065	0.044	0.058	0.197	0.339
	0.099	0.064	0.048	0.043	0.033	0.029	0.034	0.063	0.133
805	0.353	0.149	0.162	0.081	0.007	0.033	0.080	0.097	0.242
	0.088	0.053	0.051	0.034	0.027	0.027	0.040	0.049	0.111
824	0.393	0.166	0.084	0.119	0.106	0.046	0.022	0.081	0.145
	0.099	0.054	0.043	0.040	0.038	0.030	0.024	0.044	0.088
842	0.322	0.255	0.233	0.081	0.053	0.021	0.024	0.077	0.132
	0.097	0.068	0.058	0.031	0.030	0.022	0.024	0.039	0.075
861	0.405	0.269	0.228	0.142	0.051	0.084	0.025	-0.007	0.124
	0.124	0.076	0.066	0.042	0.034	0.036	0.026	0.026	0.083
879	0.569	0.288	0.078	0.103	0.087	0.040	0.033	0.013	0.176
	0.163	0.093	0.061	0.045	0.044	0.037	0.033	0.032	0.105
898	0.502	0.225	0.187	0.124	0.148	0.067	0.067	0.012	0.284
	0.125	0.065	0.055	0.035	0.041	0.031	0.028	0.023	0.094
915	0.352	0.137	0.109	0.121	0.143	0.133	0.063	0.058	0.052
	0.127	0.065	0.056	0.040	0.046	0.044	0.030	0.035	0.078
934	0.667	0.411	0.146	0.142	0.176	0.145	0.050	0.072	0.071
	0.148	0.091	0.060	0.043	0.047	0.050	0.041	0.044	0.092

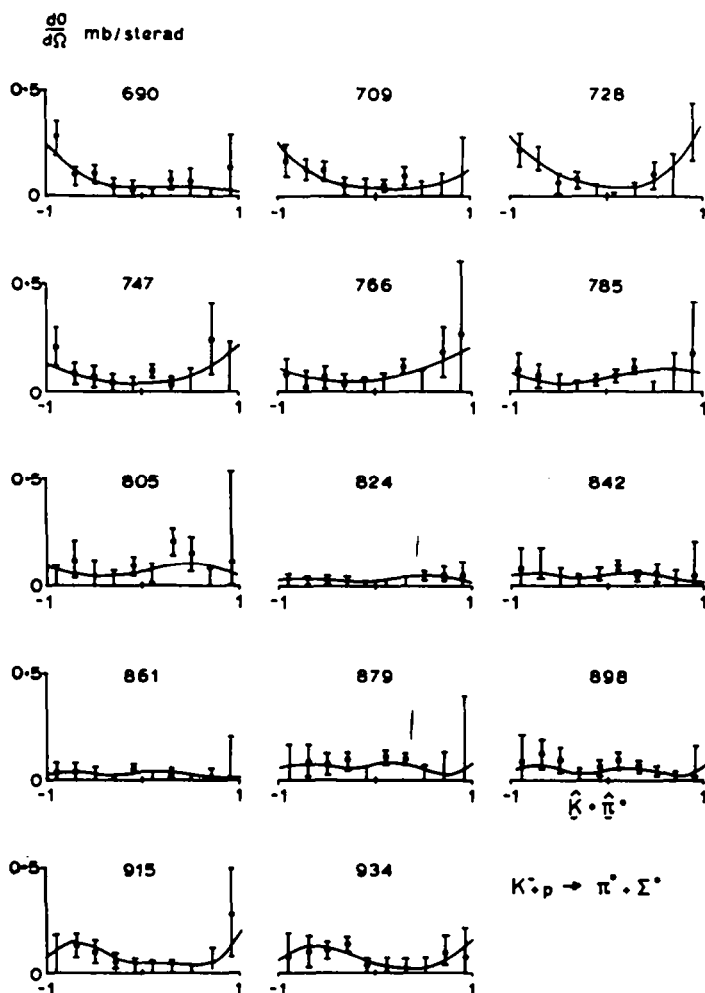


Fig. 12. The differential cross sections for the  $\Sigma^0\pi^0$  channel. The curves are from the partial wave solution.

The apparatus was triggered, however, if a  $\gamma$ -ray converted in or before the coincidence counters or a neutron interacted in these counters. Approximately 10% of the above processes caused the apparatus to trigger by conversion of  $\gamma$  rays or interaction of neutrons. The rate for no veto signal and no trigger of the apparatus is given by

$$R_{nvnt} = 0.9 I d N L \sigma_{nd}$$

Table 2  
Differential cross section for the reaction  $K^- p \rightarrow \pi^0 \Sigma^0$  as a function of the cosine of the c.m. scattering angle between the initial kaon and the final pion momenta and at fixed values of the  $K^-$  lab momentum,  $p_L$ . The bin width in  $\cos \theta_{cm}$  is  $\pm 0.10$ . The error is given beneath the value of the cross-section for each entry. The cross section is given in mb/str.

$p_L$ (MeV/c)	-0.9	-0.7	-0.5	-0.3	-0.1	+0.1	+0.3	+0.5	+0.7	+0.9
690	0.284	0.091	0.103	0.032	0.015	0.0	0.069	0.054	-0.067	0.0
	0.086	0.051	0.046	0.053	0.053	0.032	0.047	0.084	0.122	0.296
709	0.174	0.131	0.123	0.049	0.040	0.048	0.102	0.022	-0.012	0.0
	0.084	0.050	0.048	0.046	0.050	0.046	0.046	0.048	0.132	0.298
728	0.233	0.188	0.058	0.076	0.015	-0.023	0.021	0.102	0.077	0.481
	0.087	0.063	0.053	0.050	0.045	0.034	0.048	0.072	0.131	0.310
747	0.222	0.084	0.071	0.043	0.030	0.103	0.021	0.045	0.266	-0.105
	0.101	0.057	0.056	0.048	0.047	0.035	0.049	0.071	0.185	0.354
766	0.082	0.028	0.067	0.039	0.013	0.043	0.127	0.033	0.192	0.279
	0.093	0.073	0.058	0.048	0.053	0.044	0.032	0.086	0.126	0.377
785	0.095	0.077	0.035	0.004	0.052	0.075	0.127	-0.016	0.064	0.187
	0.093	0.060	0.045	0.040	0.031	0.027	0.032	0.059	0.125	0.255
805	-0.056	0.128	0.031	0.013	0.102	0.060	0.223	0.161	-0.108	0.119
	0.154	0.093	0.090	0.059	0.047	0.048	0.070	0.086	0.194	0.466
824	0.005	0.012	0.022	0.021	-0.011	0.012	0.019	0.045	0.052	0.033
	0.041	0.023	0.018	0.017	0.016	0.012	0.010	0.018	0.037	0.072
842	0.074	0.110	0.022	0.016	0.046	0.097	0.039	0.055	-0.018	-0.035
	0.110	0.077	0.066	0.035	0.034	0.025	0.027	0.044	0.085	0.257
861	0.002	0.033	0.016	-0.008	0.045	0.066	0.029	0.004	-0.003	0.091
	0.075	0.046	0.039	0.025	0.021	0.022	0.016	0.015	0.050	0.125
879	0.011	0.084	0.076	0.095	0.017	0.108	0.097	0.034	0.032	0.0
	0.156	0.089	0.059	0.044	0.042	0.036	0.031	0.031	0.101	0.427
898	0.090	0.125	0.091	0.004	0.051	0.091	0.058	0.036	-0.068	-0.043
	0.138	0.072	0.061	0.039	0.045	0.034	0.031	0.026	0.104	0.209
915	0.063	0.136	0.098	0.056	0.022	0.008	0.028	-0.009	0.048	0.314
	0.127	0.065	0.056	0.040	0.046	0.044	0.030	0.035	0.078	0.236
934	0.072	0.104	0.108	0.138	0.026	0.023	0.022	0.028	0.102	0.086
	0.128	0.079	0.052	0.037	0.040	0.043	0.035	0.038	0.079	0.139

where  $I$  is the target illumination,  $d$  is the density of the liquid hydrogen,  $L$  is the nominal length of the liquid hydrogen target,  $N$  is Avogadro's number,  $\sigma_{nd}$  is the combined cross section for the reactions giving no veto signal and no trigger, and 0.9 is the fraction of the cross section  $\sigma_{nd}$  that does not trigger the system. The rate for no veto and no trigger was then computed from rates recorded during running. Corrections were included for random coincidences (20%) and self vetoing beam particles (13%). A final value for the target illumination of 0.59 was found which agrees within error with that required to bring the CHS data and the data of this experiment together for the  $\Lambda\pi^0$  channel. No significant variation of the illumination with beam momentum was seen. Assuming a target illumination of 0.59 the differential cross sections for the  $\Lambda\pi^0$  and  $\Sigma^0\pi^0$  channels measured in this experiment are presented in tables 1 and 2 and in figs. 11 and 12. The calculation of the illumination includes various sources of error which lead to an estimate of the overall normalization error of 12% for the  $\Lambda\pi^0$  channel and 15% for the  $\Sigma^0\pi^0$  channel. The partial cross sections for the  $\Lambda\pi^0$ ,  $\Sigma^0\pi^0$ ,  $\Lambda\eta$  and  $\Sigma^0\eta$  channels appear in table 3.

### 5.2. Polynomial expansion

In the first phase of the data analysis, the differential cross sections were parameterized as polynomial expansions

$$I(x) = \frac{d\sigma}{d\Omega} \left( \frac{\lambda}{2\pi} \right)^2 \sum_{L=0}^{L_{\max}} A_L P_L(x), \quad (2)$$

**Table 3**  
Partial cross sections in mb

$p_L$ (MeV/c)	$\Lambda\pi^0$	$\Sigma^0\pi^0$	$\Lambda\eta$	$\Sigma^0\eta$
690	$2.63 \pm 0.29$	$0.73 \pm 0.13$		
709	$2.04 \pm 0.27$	$0.85 \pm 0.18$		
728	$2.10 \pm 0.26$	$1.54 \pm 0.38$	$0.41 \pm 0.24$	
747	$2.49 \pm 0.28$	$0.98 \pm 0.25$	$1.26 \pm 0.51$	
766	$3.00 \pm 0.32$	$1.14 \pm 0.49$	$0.65 \pm 0.95$	
785	$3.24 \pm 0.29$	$0.88 \pm 0.29$	$1.34 \pm 0.41$	
805	$2.24 \pm 0.27$	$0.85 \pm 0.27$	$0.02 \pm 0.51$	
824	$2.14 \pm 0.26$	$0.26 \pm 0.12$	$0.69 \pm 0.28$	
842	$2.13 \pm 0.26$	$0.51 \pm 0.19$	$0.31 \pm 0.17$	
861	$2.31 \pm 0.27$	$0.27 \pm 0.13$	$0.26 \pm 0.16$	
879	$2.37 \pm 0.37$	$0.70 \pm 0.22$	$0.43 \pm 0.24$	
898	$2.72 \pm 0.27$	$0.55 \pm 0.15$	$0.31 \pm 0.16$	
915	$1.94 \pm 0.27$	$0.96 \pm 0.21$	$0.24 \pm 0.13$	$0.75 \pm 0.32$
934	$3.09 \pm 0.30$	$0.89 \pm 0.20$	$0.46 \pm 0.20$	$1.20 \pm 0.38$

$$PI(x) = \hat{n} \left( \frac{\lambda}{2\pi} \right)^2 \sum_{L=1}^{L_{\max}} B_L P_L^1(x), \quad \hat{n} = \frac{\mathbf{k}_i \times \mathbf{k}_f}{|\mathbf{k}_i \times \mathbf{k}_f|}, \quad (3)$$

where  $P_L$  are the Legendre polynomials,  $\lambda$  is the c.m. incident wavelength,  $P$  is the polarization,  $I$  is the angular distribution, and  $x$  is the cosine of the c.m. scattering angle, that is the angle between the initial kaon and the final pion. Our results for the partial cross sections for the  $\Lambda\pi^0$  and  $\Sigma^0\pi^0$  channels are shown in fig. 13. Also shown in these figures are the results found by the CHS group [1, 2]. The dotted line is our phase shift solution.

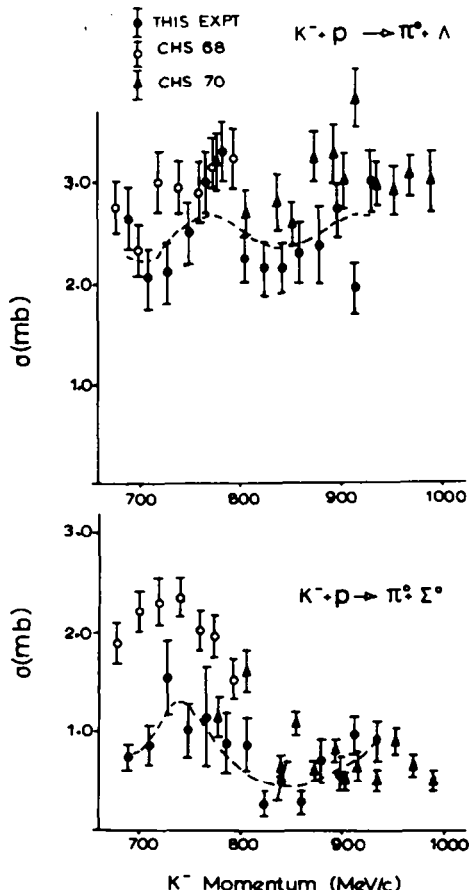


Fig. 13. The partial cross sections in mb plotted against beam momentum for the  $\Lambda\pi^0$  and  $\Sigma^0\pi^0$  channels. The partial wave solution of this paper is shown as the dashed line.

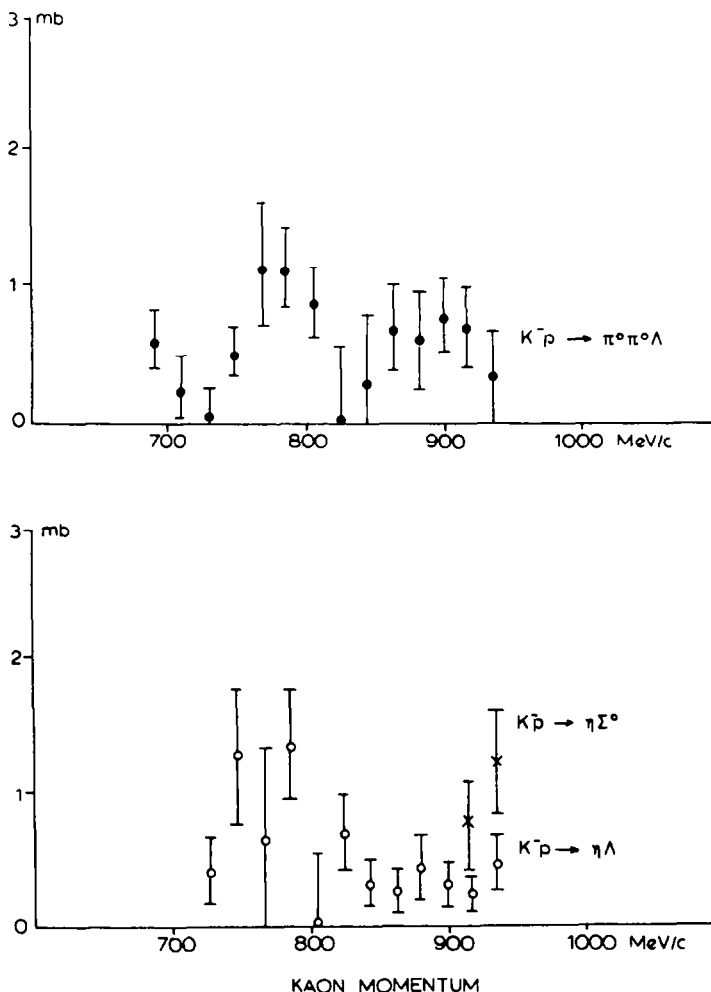


Fig. 14. The partial cross section in mb plotted against beam momentum for the  $\Lambda\eta$ ,  $\Sigma^0\eta$  and  $\Lambda\pi^0\pi^0$  channels.

The extreme forward bin is in the region where our detection efficiency is falling and the cross section is rising, so that a slight error here in the total efficiency has a large effect on the angular distribution. As a consequence the data for which  $0.8 \leq x \leq 1.0$  had large errors and these bins were omitted in the analysis.

In the  $\Sigma^0\pi^0$  channel, however, the slowest  $\Sigma^0$  that could be produced had a lab momentum of 119 MeV/c compared to 33 MeV/c for the slowest lambda. Thus the detection efficiency for the  $\Sigma^0\pi^0$  channel did not fall to zero in the most forward

bin and we have used our data throughout the full angular range. Our results for the  $\Sigma^0\pi^0$  data are also shown in fig. 13 and are again compared to those of CHS.

In a comparison of our results to those of CHS for the  $\Sigma^0\pi^0$  channel, three points stand out. Firstly, our  $A_0$  values are not in conflict with theirs for the high momentum results. Secondly, the low momentum CHS  $A_0$  values are appreciably higher than those that we find. Finally, the differential cross sections appear to differ by the presence of a flat background in the CHS angular distributions. Interpolating the CHS data to our momenta, a relative  $\chi^2$  was defined between the two data sets and a minimum in this quantity was found with the addition of a flat background of 0.75 mb to the CHS data. Notice that these differences in the  $\Sigma^0\pi^0$  channel are not affected by the uncertainty in the overall normalization. In a preliminary paper presented at the Purdue conference we showed our results with the  $\Lambda\pi^0$  channel normalized to CHS and the discrepancy is clear [6, 7].

Our results for the  $\Lambda\pi^0\pi^0$  channel are shown in fig. 14. We have not derived the  $\Sigma^0\pi^0\pi^0$  channel from the data and therefore have not corrected directly for its contamination of the  $\Lambda\pi^0\pi^0$  results. However, the  $\Sigma^0\pi^+\pi^-$  cross section is smaller than that of  $\Lambda\pi^+\pi^-$  by a factor of about seven throughout our momentum range [9]. We have assumed that a similar ratio applies to the neutral states and have made a first order correction for this small effect.

Our partial cross section results for the  $\Lambda\eta$  and  $\Sigma^0\eta$  channels are also shown in fig. 14. The  $\Lambda\eta$  data were corrected for their contamination from the  $\Lambda\pi^0$  and  $\Sigma^0\pi^0$  channels which amounted to 30% at the high momenta. Near threshold, corrections to  $\Sigma^0\eta$  are negligible. The  $\Lambda\eta$  reaction has been studied in other experiments and our results compare well with CHS [1, 10]. There are no published data for  $K^- p \rightarrow \Sigma^0\eta$ . Our data show the expected sharp rise in cross section above threshold assumed to be associated with the presence of the  $\Sigma(1750)$ .

### 5.3. Phase shift analysis

A phase shift analysis has been performed for the reactions  $K^- p \rightarrow \pi^0\Lambda$ ,  $K^- p \rightarrow \pi^0\Sigma^0$ ,  $K^- p \rightarrow \eta\Lambda$ ,  $K^- p \rightarrow \Lambda\pi^0\pi^0$ . We have used an approach similar to that of ref. [11] in which each partial wave is parameterized as a Legendre polynomial expansion in momentum up to fifth order for both real and imaginary parts,

$$\sum_{m=0}^5 a_m P_m(x), \quad x = \frac{p_{\min} + p_{\max} - 2p}{p_{\min} - p_{\max}}, \quad (4)$$

This allowed sufficient latitude to the amplitudes to follow the data while ensuring continuity between adjacent momentum points. The analysis was done for S, P, D and F waves giving seven possible waves. The phases were determined relative to well established resonances by constraining resonant waves to a Breit-Wigner energy dependence.

The procedure was to start from a set of predetermined values and keep the pa-

rameters of all but one wave fixed. The parameters for this wave were then determined and minimization proceeded for the next wave. The first wave varied was that found to be the most sensitive and the process was iterated until convergence was achieved.

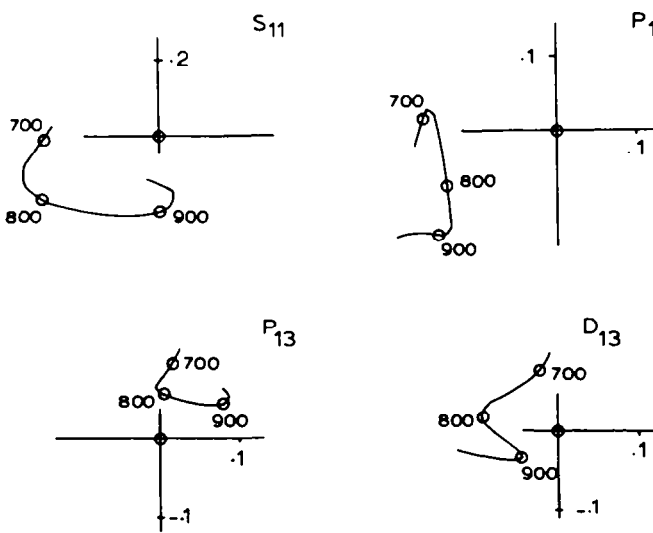
In analysing the  $\Lambda\pi^0$  channel, we have combined our data with that of CHS. It was decided to use the angular distributions from this experiment rather than the expansion coefficients because of the low apparatus detection efficiency as  $\cos\theta_{K\pi}$  approached +1.0. The analysis was therefore done using the corrected angular distributions from this experiment in the range from -1.0 to +0.8 instead of the  $A$  coefficients. We did, however, use the  $A_0$  coefficients since they contain the normalization. The  $B$  coefficients were used since they are not appreciably affected by our apparatus detection efficiency. The CHS data was used in the form of the angular distributions and the  $B$  coefficients.

The phases of the waves were determined relative to the two resonances listed in table 4. The CHS energy independent solution was parameterized in terms of Legendre polynomials and used as the starting point for the analysis. An initial  $\chi^2$  of 1200 was reduced to 659 for 560 data points. For six real and six imaginary coefficients with seven waves, two of which were fixed, we had 60 free parameters. It was found, however, that only 28 of these were sensitive in the sense that they showed significant changes in  $\chi^2$ .

The results are presented in fig. 15 which shows  $S_{11}$  and  $D_{13}$  resonant waves whose parameters are given in table 4. Thus we verify with this data the  $S_{11}$  (1750) resonance classified by the Particle Date Group as in need of clarification. We find for this resonance a mass of  $1716 \pm 10$  MeV compared to a recent world average of  $1756 \pm 24$  MeV [12]; the current PDG tables list this mass as between 1700 and 1790 [6]. The amplitude we obtained for this wave agrees, within error, with that found by other groups [12]. All parameters determined for the  $D_{13}$  resonance in our analysis are in agreement with other groups [12]. We find no evidence for resonant behaviour in the  $P_{11}$  or  $P_{13}$  amplitudes.

**Table 4**  
Results of the phase-shift analysis. Values in parentheses have been kept constant in the analysis

Channel	Wave	Mass (MeV)	Width (MeV)	Amplitude
$\Lambda\pi^0$	$S_{11}$	$1716 \pm 10$	$60 \pm 20$	$-0.28 \pm 0.05$
	$D_{13}$	(1660)	$70 \pm 20$	$+0.10 \pm 0.02$
	$D_{15}$	(1767)	(108)	(-0.26)
	$F_{15}$	(1915)	(65)	(-0.05)
$\Sigma^0\pi^0$	$S_{01}$	$1700 \pm 10$	$65 \pm 20$	$-0.28 \pm 0.05$
	$D_{03}$	$1670 \pm 10$	$30 \pm 10$	$-0.20 \pm 0.03$
	$F_{05}$	(1817)	(71)	(-0.27)
$\Lambda\eta$	$S_{01}$	(1690)	(45)	$+0.20 \pm 0.05$
	$D_{03}$	(1670)	(45)	$0.0 - +0.03$



$K^- p \rightarrow \Lambda + \pi^0$   
 Fig. 15. The partial wave amplitudes for the  $\Lambda\pi^0$  channel.

The presence of significant background complicates the estimates of these parameters and their errors. Background distorts the shape of the resonance in the Argand plot and the error estimate is sensitive to this shape. Thus the errors listed in table 4 must be regarded as approximate.

The analysis of the  $\Lambda\pi^0$  channel was repeated starting with the solution of Langbein and Wagner [13]. The resulting  $\chi^2$  at minimum, however, was somewhat worse. In this case the  $D_{15}$  and  $F_{15}$  waves were released and the solution converged on very different values. The  $S_{11}$  wave was found to move in the wrong direction and the  $D_{13}$  essentially disappeared. Other waves, although different from the previous solution, had no features of particular interest. We conclude that the solution of all waves is greatly affected by the small  $D_{15}$  amplitude of non-resonant shape as found by Langbein and Wagner.

Since the CHS results for the  $\Sigma^0\pi^0$  channel were considerably different from ours, we have used our data alone in the analysis of this reaction. The input data were again the  $A_0$ 's, the angular distributions (in this case over the full angular range), and the  $B$  coefficients. Two well established resonances, the  $D_{05}$  and  $F_{05}$ , were fixed to determine the phases with the parameters given in table 4. Starting values were taken from the CHS solution giving an initial  $\chi^2$  of 316 which reduced to 87 for 179 data points with about 30 sensitive parameters out of a total of 55.

The solution, presented in fig. 16, shows resonant behaviour in  $S_{01}$  and  $D_{03}$  waves with the parameters given in table 4. These waves had stable solutions while

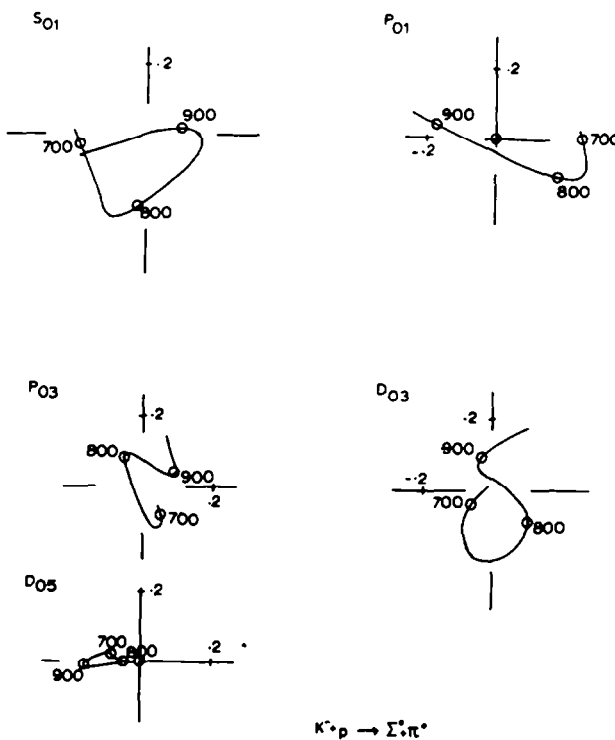
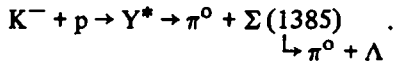


Fig. 16. The partial wave amplitudes for the  $\Sigma^0 \pi^0$  channel.

the  $P_{03}$  and  $D_{05}$  waves varied considerably with changes in the starting values. In this solution the amplitudes of the  $S_{01}$  and  $D_{03}$  are both significantly lower than the CHS solutions, an effect consistent with our smaller cross section. We find a mass of 1700 for the  $S_{01}$  compared to 1670 from the PDG table [6] and our width is somewhat larger than accepted values. Our determinations of mass and width for the  $D_{03}$  are in agreement with accepted values.

The  $P_{01}$  amplitude, while not very stable in this analysis, has considerable spread between 800 and 900 MeV/c suggestive of a resonance. However, though this constitutes no positive evidence for a  $P_{01}$  resonance, it could be present as a very broad effect centred at 1720 MeV with a large amplitude.

We have analysed our data for the  $\Lambda \pi^0 \pi^0$  channel assuming it to be dominated by  $\Sigma(1385)$  production, thus



The analysis of the  $Y^*$  was done assuming the  $S_{01}$ ,  $D_{03}$  and  $F_{05}$  waves to be reso-

nant and allowing for background in  $S_{01}$  and  $P_{01}$  states. The  $F_{05}$  was taken as the fixed resonance to establish the phases. A good fit was then obtained by fixing the mass and width of the  $D_{03}$  but allowing the  $S_{01}$  to go free. The amplitudes of the  $S_{01}$  and  $D_{03}$  were +0.14 and +0.16. The amplitude of the  $S_{01}$  agrees well with the prediction of Fairman and Plane [14].

In analysing the  $\Lambda\eta$  channel we again assumed the  $S_{01}$ ,  $D_{03}$  and  $F_{05}$  waves to be resonant and that we could parameterize any background as S-wave. The masses and widths of all three resonances were fixed and the amplitudes allowed to vary. Reasonable fits were obtained assuming either a constant or linearly varying background. The results appear in table 4. The amplitudes found for  $D_{03}$  and  $S_{01}$  were +0.025 and +0.20, the latter consistent with the values found by CHS [15] and Kim [16]. Although +0.025 is the best value for the  $D_{03}$  amplitude, it can be reduced to zero if one allows a linear background. The results were found to be insensitive to the  $F_{05}$  parameters.

We would like to acknowledge our indebtedness to Prof. D.H. Wilkinson and the staff of the Oxford Nuclear Physics Laboratory and to Dr. G.H. Stafford and the staff of the Rutherford High Energy Laboratory. We are particularly grateful to the Oxford Spark Chamber Group scanners and their supervisors Diana Crowe, Mag Simmons and Jane Hammond. We wish to express our appreciation to Drs. A. Engler and G. Culligan for their assistance. Finally, we would like to thank J.H. Bibby and his staff for their considerable contribution.

## References

- [1] R. Armenteros, M. Ferro-Luzzi, D.W.G.S. Leith, R. Levi-Setti, A. Minten, R.D. Tripp, H. Filthuth, V. Hepp, E. Kluge, H. Schneider, R. Barloutaud, P. Granet, J. Meyer and J.P. Porte, *Nucl. Phys.* B8 (1968) 233.
- [2] R. Armenteros, P. Baillon, C. Bricman, M. Ferro-Luzzi, E. Pagiola, J.O. Petersen, D.E. Plane, N. Schmitz, E. Burkhardt, H. Filthuth, E. Kluge, H. Oberlack, R.R. Ross, R. Barloutaud, P. Granet, J. Meyer, J.P. Porte and J. Prevost, *Nucl. Phys.* B21 (1970) 15.
- [3] L. Bertanza, A. Bigi, R. Carrara, R. Casali, R. Pazzi, D. Berley, E.L. Hart, D.C. Rahm, W.J. Willis, S.S. Yamamoto and N.S. Wong, *Phys. Rev.* 177 (1968) 2036.
- [4] W.M. Smart, A. Kieran, G.E. Kalmus and R.E. Ely, *Phys. Rev. Letters* 17 (1966) 556.
- [5] T. Dombeck, W.W.M. Allison, J. Campbell, Y. Cho, M. Derrick, R. Engelmann, T. Groves, T.P. Wangler, N.S. Wong, and D. Koetke, *Phys. Rev. D7* (1973) 1331; R.Y.L. Chu, G.W. London, Y.P. Yu, D. Boyd, T. Beggs, D.J. Candlin, A.T. Goshaw, H.W.K. Hopkins, W. Venus, P. Alibran, S. Kahn, J.P. Lowys, R. Stump, S.P. Wuthrich, J. Colas, C. Farwell, A. Ferrer, E. Gombosi, T. Hofmokl, J. Six, D. Gamba, A. Marzari, A. Romero and A.E. Werbrouck, paper reviewed by D.E. Plane, *Purdue Conf. on baryon resonances*, April 1973.
- [6] N. Barash-Schmidt, A. Barbaro-Galtieri, C. Bricman, V. Cahlioupka, R.L. Kelly, T.A. Lasinski, A. Rittenberg, M. Roos, A.H. Rosenfeld, P. Soding, T.G. Trippe, *Rev. Mod. Phys.*, vol. 45 no. 2, part II, April 1973.

- [7] D.F. Baxter, I.D. Buckingham, I.F. Corbett, P.A. Dunn, J. McL. Emmerson, A. Engler, J. Garvey, F. Hart, G. Hughes, C.M.S. Jones, R. Maybury, N. Middlemas, P.R. Norton, T.W. Quirk, J.A. Scheid and A.M. Segar, Proc. Purdue Conf. on baryon resonances, 1973.
- [8] D.E. Plane, Proc. Purdue Conf. on baryon resonances, 1973.
- [9] E. Flaminio, J.D. Hansen, D.R.O. Morrison and N. Tovey, CERN/HERA 70-6.
- [10] R. Armenteros, P. Baillon, C. Bricman, M. Ferro-Luzzi, H.K. Nguyen, V. Pelosi, D.E. Plane, N. Schmitz, E. Burkhardt, H. Filthuth, E. Kluge, H. Oberlack, R.R. Ross, R. Barloutaud, P. Granet, J. Meyer, J.L. Narjoux, F. Pierre, J.P. Porte and J. Prevost, Nucl. Phys. B8 (1968) 183.
- [11] P.J. Litchfield, Rutherford Laboratory RPP/H/66.
- [12] A. Barbaro-Galtieri, Proc. 16th Int. Conf. on high energy physics, Chicago-Batavia, Illinois (1972).
- [13] W. Langbein and F. Wagner, Nucl. Phys. B47 (1972) 477.
- [14] D. Faiman and D.E. Plane, CERN Th. 1549.
- [15] CHS Collaboration, Proc. Int. Conf. on elementary particles, Lund, 1969 (Berlingska Boktryckeriet, Lund, Sweden, 1969) p. 425.
- [16] J.K. Kim, Phys. Rev. Letters 27 (1971) 356.